JOURNAL OF SOLID STATE CHEMISTRY 115, 332–346 (1995)

Layered Cuprates with the T* Structure: Structural and Conducting Properties

Alexandros Lappas and Kosmas Prassides[1]

School of Chemistry and Molecular Sciences, University of Sussex, Brighton BN1 9QJ, United Kingdom

Received April 1, 1994; accepted August 8, 1994

The structural and conducting properties of the oxide $La_{1.2}Tb_{0.8}CuO_{4+\delta}$ and its Sr^{2+} and Ce^{4+} lightly doped derivatives (T* phases) are examined as functions of temperature. The properties of the isostructural heavily doped $La_{1.0}Dy_{0.8}Sr_{0.2}CuO_4$ are also investigated. High-resolution powder neutron structural results confirm that the correct space group is tetragonal *P4/nmm*, with no low symmetry distortions apparent to low temperatures and an essentially perfect lanthanide ordering into two crystallographically inequivalent sites. Excess oxygen (its presence also revealed by thermogravimetric analysis measurements) is accommodated as an O^{2-} ion in the interstitial space defined by the lanthanum ion bilayers in the rock-salt part of the unit cell. No excess oxygen is needed to stabilize the T* structural type for large Sr^{2+} doping levels, as in $La_{1.0}Dy_{0.8}Sr_{0.2}CuO_4$. Analysis of the resistivity data shows the occurrence of two-dimensional variable-range hopping, implying that the electronic states at the Fermi level are localized. A crossover to a three-dimensional hopping mechanism occurs with increased carrier density in $La_{1.0}Dy_{0.8}Sr_{0.2}CuO_4$ at low temperatures, with high temperature transport dominated by small-polaron behavior. The charge carriers are essentially confined within the boundaries of the unit cell for all compositions.

INTRODUCTION

Superconducting ceramic cuprates are invariably characterized by the presence of CuO_2 layers, formed by corner-sharing CuO_4 units. Particularly attractive to study as prototypical systems for the microscopic mechanism of high-T_c superconductivity are the single-layer cuprates of stoichiometry A_2CuO_4, in which the copper–oxygen layers may be part of (i) strongly elongated octahedral CuO_6 units (O/T phases, $(La,Sr)_2CuO_{4-\delta}$) (1), (ii) square-planar CuO_4 units (*T'* phases, $(Nd,Ce)_2CuO_{4-\delta}$) (2), or (iii) square-pyramidal CuO_5 units (T* phases, $(Nd,Ce,Sr)_2CuO_{4-\delta}$) (3). Despite their apparent simplicity, these systems have shown remarkably rich structural, magnetic, and conducting phase diagrams as a function of temperature, cation dopant level, and oxygen nonstoichiometry. In brief, changes in the formal Cu oxidation state and the filling of the conduction band are achieved through either chemical doping of the lanthanide supporting layers or oxygen nonstoichiometry ($\delta \neq 0$) (4). At the same time, an intimate relationship exists between the magnetic and (super)conducting properties of these systems with the antiferromagnetic long-range order found for the undoped parent materials always removed upon electron- or hole-doping before the onset of superconductivity (5–7).

The structural properties of the $(La,M)_2CuO_{4\pm\delta}$ (M = Ca, Sr, Ba) and $(Nd,M)_2CuO_{4-\delta}$ (M = Ce, Th) families of cuprates have been exhaustively studied. La_2CuO_4 adopts the tetragonal (T) K_2NiF_4 structure (space group *I4/mmm*) at elevated temperatures; upon cooling, it undergoes at ~530 K a second-order phase transition to an orthorhombic (O) structure (space group *Cmca*) (8), driven by the cooperative rigid tilting of the elongated CuO_6 octahedra along the [110] direction of the tetragonal unit cell. The CuO_2 layers are separated along the *c*-axis by rock salt La_2O_2 bilayers in which La^{3+} is coordinated to nine O^{2-} ions (CN = 9). Doping with divalent cations has the effect of reducing the T → O phase transition temperature which for $La_{1.85}Sr_{0.15}CuO_4$ occurs at ~180 K (1). An additional structural complication is found for Ba-doped systems, in which a second transition to a low-temperature tetragonal phase (LTT, space group $P4_2/ncm$) with a detrimental effect on superconductivity has been identified over a narrow composition range in the vicinity of $La_{1.875}Ba_{0.125}CuO_4$ (9). Moreover, La_2CuO_4 can easily accommodate excess oxygen up to $\delta \sim 0.08$; at larger oxygen excess, phase separation occurs into a stoichiometric insulating phase (space group *Cmca*) and an oxygen-rich superconducting phase (space group *Fmmm*) (10). Nd_2CuO_4 adopts a different tetragonal (T') structure (space group *I4/mmm*), characterized by the displacement of the apical oxygens of the La_2CuO_4 structure to the tetrahedral interstices, resulting in the formation of fluorite Nd_2O_2 bilayers with Nd^{3+} coordinated to eight O^{2-} ions (CN = 8). The Cu coordination is now fourfold, strictly square-planar (11). This structure is very robust, persisting undistorted

[1] To whom correspondence should be addressed.

0022-4596/95 $6.00

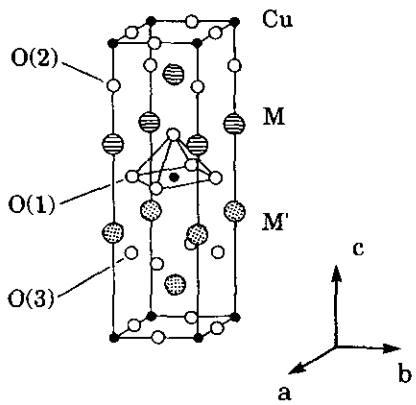

FIG. 1. Unit cell of the ideal T* structural type of cuprates with stoichiometry $(M, M')_2CuO_4$. The two symmetry-inequivalent rare-earth sites are shown: a ninefold M and an eightfold coordinated M' site.

down to the lowest temperatures studied (7). Similarly, doping with tetravalent ions does not lead to any deviations from tetragonal symmetry (12).

A third structural variations encountered for $(M,M')_2CuO_4$ compositions in which M and M' represent different lanthanide ions is the so-called T* phase. This is observed when the size difference between M and M' is sufficiently large to lead to ordering at the lanthanide sites in the unit cell. Thus, this structural type has two independent rare-earth sites: a ninefold M and an eightfold coordinated M' site. The unit cell (space group $P4/nmm$) may be regarded as arising from fusing together half of the T and T' structural motifs, resulting in a fivefold square-pyramidal coordination of copper. The CuO_2 layers are now separated along the c-axis by alternating rock-salt- and fluorite-type lanthanide bilayers (Fig. 1). The T* structural variant was first suggested for a superconducting oxide with composition $Nd_{1.32}Ce_{0.27}Sr_{0.41}CuO_4$ (13). The formally undoped T* phase occurs as a single phase only over a very narrow range of compositions and only for Tb and Dy [$La_{2-x}Tb_xCuO_4$, $x \sim 0.6$–0.8 and $La_{2-x}Dy_xCuO_4$, $x \sim 0.8$–0.9] (14–17). However, its thermodynamic stability is improved upon Sr^{2+} doping and as a consequence, a much wider composition range with formal stoichiometry $La_{2-x-y}Ln_xSr_yCuO_4$, (Ln = Nd, Sm, Eu, Gd, Tb, and Dy) can be synthesized (15, 16).

In this paper, we report a systematic examination of the structural and electron transport behavior in the $La_{2-x}Tb_xCuO_{4+\delta}$ model system and its Sr^{2+} and Ce^{4+} doped derivatives. We have used conductivity measurements and high-resolution powder neutron diffraction to investigate in detail these properties as they vary with changes in both cation dopant and oxygen concentration. A simultaneous investigation of the magnetic properties of these systems by employing neutron diffraction and muon spin relaxation (μSR) measurements will be reported elsewhere (18, 19).

EXPERIMENTAL

Polycrystalline powders with highly homogeneous dopant distributions were synthesized by employing a solution-based citrate sol–gel technique (6). Single-phase samples (in ~10-g quantities) of $La_{1.2-x}Tb_{0.8}Sr_xCuO_{4+\delta}$ (x = 0.0, 0.01, 0.03, and 0.05), $La_{1.2}Tb_{0.8-y}Ce_yCuO_{4+\delta}$ (y = 0.01 and 0.03), and $LaDy_{0.8}Sr_{0.2}CuO_{4-\delta}$ were prepared in this way. Firing temperatures of 650°C (12 hr) and 1000°C (with repeated regrinding, pelletizing, and sintering cycles) were employed. All heating and cooling cycles (both at 1°C/min rates) were performed in flowing oxygen. Phase purity of the samples was confirmed by powder X-ray diffraction with a Siemens D5000 diffractometer.

The oxygen stoichiometry of the materials was determined by thermogravimetric reduction in flowing 5% H_2–95% Ar mixture. Weight versus temperature profiles were obtained with either a Perkin–Elmer TGA-7 or a Stanton–Redcroft STA 1500 system. The weight loss curve for $La_{1.2}Tb_{0.8}CuO_{4+\delta}$ is presented in Fig. 2; 57.76 mg of the sample was placed in a platinum crucible and heated at a rate of 2.5°C/min to 830°C. The weight of the compound decreased gradually between ~300 and ~500°C, featuring a small plateau around 380°C. The oxygen conentration was evaluated by describing the overall reduction by the reaction

$$La_{1.2}Tb_{0.8}CuO_{4+\delta} + (1+\delta)H_2 \rightarrow 0.6La_2O_3 + 0.4Tb_2O_3 + Cu + (1+\delta)H_2O. \quad [1]$$

According to this scheme, all Tb present is in the trivalent state. There is, however, evidence from near-edge X-ray absorption studies that a significant proportion of Tb^{4+} ions (20%) is present (20). Although long X-ray diffraction

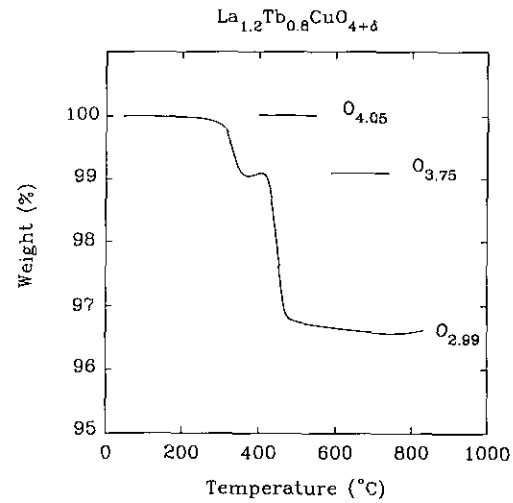

FIG. 2. Thermogravimetric reduction weight-loss curve for $La_{1.2}Tb_{0.8}CuO_{4+\delta}$.

TABLE 1
Thermogravimetric Analysis Results for the $La_{1.2-x}M'_{0.8}Sr_xCuO_{4+\delta}$ Samples Studied

M'	x	δ
Tb	0.0	0.05(3)
Tb	0.01	0.02(6)
Tb	0.03	0.03(4)
Tb	0.05	0.01(4)
Dy	0.2	−0.07(6)

scans were performed on the decomposition products, we were unable to eliminate the possibility that oxides of Tb with valency greater than 3+ (e.g., Tb_4O_7, TbO_2, etc.) were present in the products. We thus view the values of δ determined from the TGA measurements as a lower limit. The inflection point of the weight loss versus temperature profile at 375°C (Fig. 2), indicates the existence of an intermediate phase with reduced oxygen content and formal stoichiometry $La_{1.2}Tb_{0.8}CuO_{3.75}$. A similar oxygen content has been reported before for the oxygen-deficient $La_2CuO_{3.67}$ phase (21) and its $La_2Co_{0.25}Cu_{0.75}O_{3.69}$ solid solution with cobalt (22). A somewhat different procedure was employed for the oxygen determination in the remaining Sr^{2+} and Ce^{4+} doped T*-phases: rapid initial heating (40°C/min) in an inert atmosphere (99.95% Ar) to 650°C was followed by constant temperature heating in a reducing atmosphere (5% H_2–95% Ar). We were, however, unable to determine reliably the oxygen content of the Ce^{4+}-doped phases, principally because of uncertainties in the Ce oxidation state in the reduction products. The reliably determined oxygen compositions are collected in Table 1. Similar Cu valences (>+2) have been reported (23) for an air-fired sample with stoichiometry $La_{1.0}Tb_{0.8}Sr_{0.2}CuO_{3.97}$ and a $La_{1.13}Tb_{0.81}Pb_{0.06}CuO_{4.01}$ single crystal. Increasing hole doping results in reduced oxygen uptake, with oxygen vacancies appearing at high doping levels (20).

Preliminary two-probe room temperature transport measurements of samples with typical dimensions of 8.5 × 4.5 × 0.5 mm^3, gave large resistances of the order of kΩ. As a consequence, electrical conductivity measurements were performed between 300 and 4.2 K only with the two-probe technique in an Oxford Instruments CF200 cryostat with a Keithley digital multimeter. Tin wire and silver paint were used to make the electrical contacts onto samples cut from sintered (600°C, 16 hr) pellets with a diamond saw.

High resolution powder neutron diffraction data for $La_{1.2}Tb_{0.8}CuO_{4+\delta}$ were collected on the HRPD diffractometer (Rutherford Appleton Laboratory, United Kingdom) in an "orange" cryostat at 4.2 K. The high intensity 1-m sample position was used and data were collected over a time-of-flight range of 34.0–104.0 msec, corresponding to a d-spacing range of 0.70–2.15 Å. A 9-hr run at 20 μA/hr current provided excellent statistics. The raw data were normalized to the incident beam and corrected with a standard vanadium run in order to account for detector efficiency. Diffraction profiles of $La_{1.2-x}Tb_{0.8}Sr_xCuO_{4+\delta}$ (x = 0.03, 0.05), $La_{1.2}Tb_{0.77}Ce_{0.03}CuO_{4+\delta}$, and $LaDy_{0.8}Sr_{0.2}CuO_{4-\delta}$ were obtained on the high-resolution D2b diffractometer (Institut Laue–Langevin, Grenoble) with a mean wavelength λ = 1.5946 Å. The instrument was operated in its high-intensity mode and data were collected in the angular range 2θ = 0°–160°, in steps of 0.05°. The samples were mounted in cylindrical vanadium cans (o.d. = 5–7 mm), placed in a standard (orange) liquid helium cryostat and cooled to 5 K. Full diffraction profiles were obtained in 8–10 hr, with excellent signal to noise ratios. Room temperature data, with the sample kept inside the cryostat, were also collected for $La_{1.2}Tb_{0.77}Ce_{0.03}CuO_{4+\delta}$. A short 2-hr empty cryostat run was also performed. The raw data were merged and normalized to a standard vanadium run with standard ILL programs (24). After manual background subtraction, profile refinements were performed using the Rietveld profile method (25), and incorporating a pseudo-Voigt function peak shape description (26).

RESULTS

(a) *Conductivity*

Since all the samples were very resistive, their resistance was measured only over a limited temperature range. The more conducting $LaDy_{0.8}Sr_{0.2}CuO_{4-\delta}$ was fol-

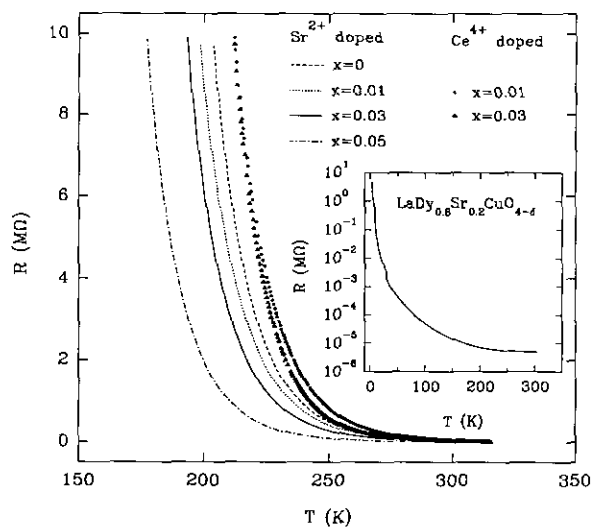

FIG. 3. Temperature dependence of the electrical resistance of the samples $La_{1.2-x}Tb_{0.8}Sr_xCuO_{4+\delta}$ and $La_{1.2}Tb_{0.8-x}Ce_xCuO_{4+\delta}$. The $LaDy_{0.8}Sr_{0.2}CuO_{4-\delta}$ data are shown in the inset.

lowed down to 3.5 K. They all exhibited semiconducting behavior with a sharp upturn in resistance (Fig. 3) that moved to lower temperatures with increasing Sr^{2+} doping level (x). Increased Sr^{2+} content was also accompanied by reduced electrical resistance. Initial analysis of the data was performed by assuming a simple Arrhenius equation of the form

$$\rho = \rho_0 \exp\left(\frac{E_a}{k_B T}\right), \qquad [2]$$

where ρ is the resistivity of the sample, ρ_0 a preexponential constant, and E_a the activation energy. However, plots of the logarithm of the resistivity against inverse temperature (T^{-1}) were not linear. As this simple model proved unsatisfactory, we examined the validity of more complex alternatives for the temperature dependence of the resistivity. The antiadiabatic small-polaron model (27) which includes a temperature-dependent polaron mobility term that had been applied before to describe satisfactorily the conducting behavior of the $La_{2-x}Sr_xCuO_{4-\delta}$ systems ($x = 0.0$–0.06) (6) was next used to analyze the data

$$\rho = \rho_0 T^{3/2} \exp\left(\frac{E_a}{k_B T}\right). \qquad [3]$$

Plots of $\ln(\rho/T^{3/2})$ against inverse temperature (T^{-1}) showed marked curvature, except for the $LaDy_{0.8}Sr_{0.2}CuO_{4-\delta}$ system at temperatures higher than 100 K, for which a hopping energy $E_a = 53.8(1)$ meV was derived for the polaron motion (Fig. 4d).

We then attempted to analyze the data with the Mott variable-range-hopping (VRH) model (28) in which charge transport occurs by thermally assisted hopping of electrons (or holes)—without any excursion to the conduction band—between states localized near randomly distributed potential fluctuations ("traps"). Excellent agreement with the experimental data was observed after least-squares fitting to the stretched-exponential form (Fig. 4):

$$\rho = \rho_0 \left(\frac{T}{T_0}\right)^{1/2} \exp\left[\left(\frac{T_0}{T}\right)^{\nu}\right], \qquad [4]$$

where $0 < \nu < 1$, with the exponent ν readily determined from the fitting procedure. Equation [4] corresponds to the general case of an arbitrary spatial dimensionality (d) of the hopping process, with $\nu = 1/(d+1)$ (29). We obtained average value for the exponent ν of 0.32 ± 0.03 for $La_{1.2}Tb_{0.8}CuO_{4+\delta}$ and its "lightly" doped ($x = 0.01$, 0.03, and 0.05) Sr^{2+} and Ce^{4+} derivatives; this is remarkably close to the $\nu = 1/3$ value, appropriate for two-dimensional VRH conduction. On the other hand, a value of $\nu = 0.22 \pm 0.03$ was extracted for $LaDy_{0.8}Sr_{0.2}CuO_{4-\delta}$ in the temperature range $30 \leq T \leq 100$ K, implying a crossover to 3D-VRH ($\nu = 1/4$) with increased carrier densities. The constants T_0, given for 3D-VRH by $T_0 = \beta/k_B\, N(E_F)\, \xi^3$ and for 2D-VRH by $T_0 = \beta/k_B\, N(E_F)\, \xi^2$, were also determined from the fits. $N(E_F)$ is the density of states at the Fermi level, ξ the localization radius of the states near the Fermi level, and $\beta \approx 21$ (3D) or $\beta \approx 14$ (2D). Table 2 summarizes the results of the analysis of the conductivity data of all the T* materials studied.

(b) *Powder Neutron Diffraction*

(i) *Profile refinement of* $La_{1.17}Tb_{0.8}Sr_{0.03}CuO_{4+\delta}$. The neutron diffraction profile of this sample, collected at 5 K with a wavelength 1.5946 Å, was characterized by an excellent signal-to-noise ratio. We thus used it to explore in detail the validity of several structural models proposed for the T* structural variants and, at the same time, attempt to elucidate certain subtle features associated with them, such as cation site ordering and oxygen site occupancies. Our Rietveld refinements were initiated in the centrosymmetric space group $P4/nmm$ with all atoms in the unit cell initially occupying their normal lattice sites. The first refinement steps incorporated a scale factor, a zero-point error, the lattice constants, the fractional coordinates of the atoms, and the Gaussian (U, V, and W) and Lorentzian (η) components of the pseudo-Voigt peak-shape function. Weak peaks arising from impurity phases (La_2O_3 and CuO) and scattering from the aluminum walls of the cryostat (as confirmed from the empty cryostat run) were excluded from the refinement. During the initial cycles of the Rietveld analysis, and in accord with the nominal composition of the sample, it was assumed that the M-sites had a fixed occupancy of 97% La^{3+}–3% Sr^{2+}, and the M' sites 20% La^{3+}–80% Tb^{3+}. Such a hypothesis, consistent with the relative ionic sizes of the atoms present in the unit cell (30, 31), resulted in chemically reasonable positional parameters for all the atoms. In addition, copper and oxygen sites were treated as fully occupied. Following the refinement of isotropic temperature factors for all the atoms, stable refinement was quickly obtained with $R_{wp} = 0.113$ and $R_I = 0.072$. However, unusually large thermal vibrations [$B_{iso} = 2.88(9)$ Å^2] were encountered for the apical oxygen O(2) of the CuO_5 square pyramids at (1/4, 1/4, z). Anisotropic thermal vibrations were then introduced for both the rare-earth and the oxygen sites, resulting in improved fit quality ($R_{wp} = 0.093$, $R_I = 0.049$). Large vibrations were also evident now for the basal plane oxygens within the plane. A similar situation was reported (10) for $La_2CuO_{4+\delta}$ but in that case the basal plane oxygens exhibited large thermal displacements perpendicular to the plane itself. Unconstrained

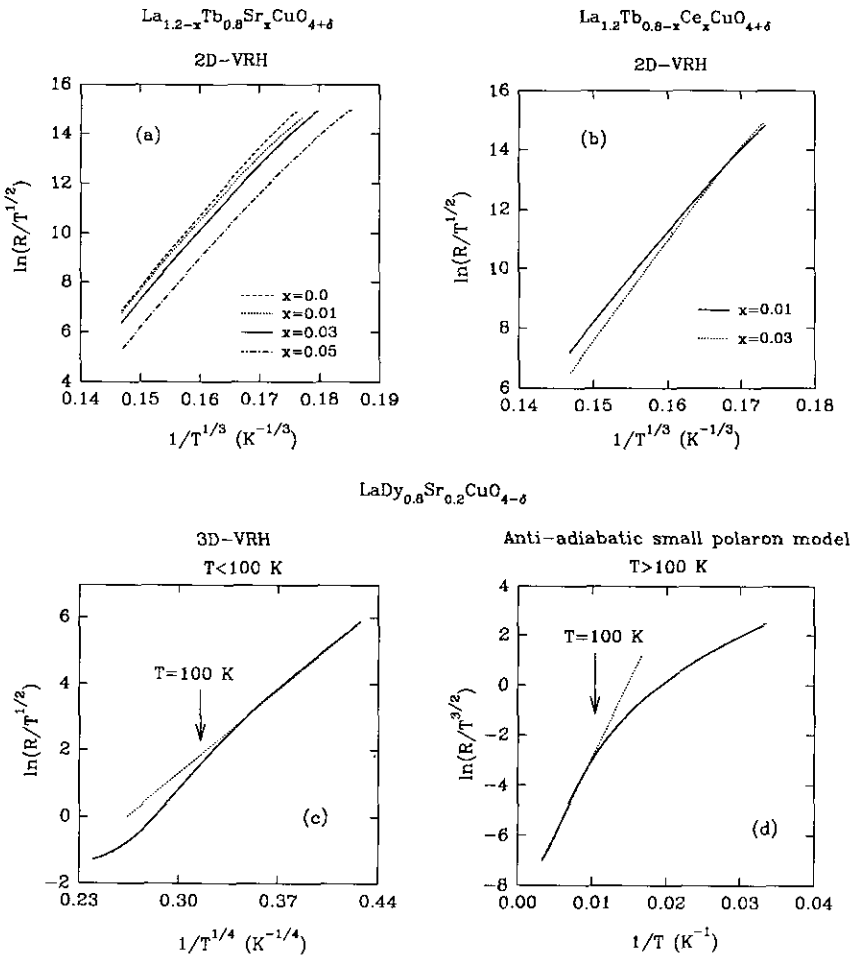

FIG. 4. Temperature dependence of the electrical resistance, showing two-dimensional variable-range-hopping (2D-VRH) for samples (a) $La_{1.2-x}Tb_{0.8}Sr_xCuO_{4+\delta}$ and (b) $La_{1.2}Tb_{0.8-x}Ce_xCuO_{4+\delta}$, and three-dimensional VRH at $T \leq 100$ K for (c) $LaDy_{0.8}Sr_{0.2}CuO_{4-\delta}$. A plot (d) appropriate for the antiadiabatic small polaron model at higher temperatures for $LaDy_{0.8}Sr_{0.2}CuO_{4-\delta}$ is also shown.

refinement of the oxygen site occupancies gave values close to the *stoichiometric* ones within experimental error.

The unusually large thermal parameters of the apical oxygens O(2) were taken as the signature of some form of positional disorder within the rock-salt type $[(La,Sr)O]_2$ layers. Sawa *et al.* (3) had reported even larger values of $B_{iso} = 3.55$ Å^2 in the case of $(Nd,Ce,Sr)_2CuO_4$ and had rationalized such a behavior in terms of short Cu–O(2) and *M*–O(2) bonds parallel to the [001] direction, together with a random distribution of Nd, Ce, and Sr atoms at the *M*-site. An alternative explanation was invoked by Izumi *et al.* (30) who proposed that the apical oxygens are displaced from the "ideal" 2*c* lattice site (1/4, 1/4, *z*) to the less symmetrical 8*j* site (*x*, *x*, *z*). Incorporation of such a "splitting" of the O(2) atoms into four equivalent sites in our refinements led to smaller isotropic temperature factors [$B_{iso} = 1.2(1)$ Å^2] and an improved fit quality. We thus continued the Rietveld analysis within this structural model by refining additional profile and structural parameters. Improvement in the description of the peak shape was achieved by using an asymmetry parameter at low angles. Reasonable isotropic temperature factors, $B_{iso} = 0.50(2)$ Å^2, resulted for the copper ions at the 2*c* sites. Anisotropic thermal vibrations were allowed for all the other atoms, except for O(2). The positional parameters for the O(2) ions rapidly converged to (*x*, *x*, *z*), $x = 0.2931(5)$, $z = -0.4286(3)$ with a thermal parameter $B_{iso} = 1.37(9)$ Å^2. We also attempted to refine the relative occupancies (*n*) of the cations at the *M* (La(1), Sr) and *M'* (La(3), Tb) sites and the occupancy factors of the three crystallographically inequivalent oxygen atoms. Initial unconstrained refinements of the La(1) and La(2) occupancies showed that the overall nominal stoichiometry of the material was conserved within one estimated standard deviation. Keeping $n_{La(1)} + n_{La(2)} = 1.17$ and $n_{Sr} = 0.03$, the Tb occupancy refined to $n_{Tb} = 0.81(1)$. Thus, within experimental error, the majority of La^{3+} ions

TABLE 2

Room-Temperature Resistivity (ρ_{300}) and Fitting Parameters (ν, ρ_0, and T_0) Extracted from the Variable-Range-Hopping Fits to the Conductivity Data of the T* Phases Studied and the Small-Polaron Parameters for La $Dy_{0.8}Sr_{0.2}CuO_{4-\delta}$ in the Range 100 K < $T \leq$ 305 K

T* phases	T (K)	ν	ρ_0 (10^{-10} Ω cm)	T_0 (10^7 K)	ρ_{300} (10^5 Ω cm)
$La_{1.2}Tb_{0.8}CuO_{4+\delta}$	180–315	0.32(3)	0.955	3.16	2.675
$La_{1.19}Tb_{0.8}Sr_{0.01}CuO_{4+\delta}$	180–315	0.32(3)	5.558	2.90	1.545
$La_{1.17}Tb_{0.8}Sr_{0.03}CuO_{4+\delta}$	170–315	0.32(3)	3.674	3.07	2.034
$La_{1.15}Tb_{0.8}Sr_{0.05}CuO_{4+\delta}$	155–315	0.32(3)	1.381	3.00	0.500
$La_{1.2}Tb_{0.79}Ce_{0.01}CuO_{4+\delta}$	190–315	0.32(3)	0.658	3.28	3.216
$La_{1.2}Tb_{0.77}Ce_{0.03}CuO_{4+\delta}$	190–315	0.33(2)	0.012	3.57	4.419
$LaDy_{0.8}Sr_{0.2}CuO_{4-\delta}$	30–100	0.22(3)	8.921×10^8	1.48	—
	100–305	Small polaron	4.810×10^6	—	2.076×10^{-4}

($n_{La(2)}$ = 0.961(3)) occupied the M site, while the smaller Tb^{3+} and the remaining La^{3+} ions ($n_{La(2)}$ = 0.209(3)) preferred the M' site (R_{wp} = 0.085, R_I = 0.040). We also searched at this stage for deviations from ideal occupation of the oxygen sites. It had been reported (23) that, while the O(1) and O(2) sites were fully occupied in $LaTb_{0.8}Sr_{0.2}CuO_{4-\delta}$, the O(3) site was incompletely filled ($n_{O(3)}$ = 0.960(8)). In contrast, Izumi *et al.* (30) reported O(2) deficiency for both oxidized (superconducting) and nonsuperconducting $Nd_{1.32}Sr_{0.41}Ce_{0.27}CuO_{4-\delta}$ phases, with $n_{O(2)}$ = 0.926(4). We thus refined all three oxygen site occupancies, being careful to avoid correlations with the thermal parameters. At the same time, n_M and n_M' were fixed to their earlier refined values, while their anisotropic temperature factors were allowed to vary. The analysis (R_{wp} = 0.084, R_I = 0.039) showed the absence of any significant concentration of oxygen vacancies ($n_{O(1)}$ = 2.007(8), $n_{O(2)}$ = 1.002(8), and $n_{O(3)}$ = 1.02(1)).

An alternative explanation for the positional disorder of the O(2) oxygens was invoked by Lightfoot *et al.* (31) who encountered a similar situation in the fluorine-rich T* phase $La_{1.25}Dy_{0.75}CuO_{3.75}F_{0.5}$ and interpreted their results in terms of excess anions accommodated in the unit cell. We thus attempted to investigate such a possibility for $La_{1.17}Tb_{0.8}Sr_{0.03}CuO_{4+\delta}$. In this model the oxygen defect was introduced in the interstitial space defined by the rock-salt type $(La,Sr)_2O_2$ layers, in a way similar to other oxygen-rich phases such as $La_2CuO_{4+\delta}$ (10), $La_2NiO_{4.18}$ (32), and $La_2Co_{0.75}Cu_{0.25}O_{4.16}$ (22). In contrast to the orthorhombic symmetry necessary to describe the distorted K_2NiF_4-type structures of these oxygen-rich systems, no lowering of symmetry was necessary to accommodate the *small* (as expected from the TGA results) amount of excess oxygen (starting value δ = 0.05). The refinement was thus continued by "displacing" O(2) to the 8*j* sites and introducing an oxygen defect O(4) in the 4*f* sites (3/4, 1/4, z). Constraining its thermal parameter to B_{iso} = 1.0 Å^2, we achieved rapid convergence with $z_{O(4)}$ =

TABLE 3

Final Structural Parameters Derived from Rietveld Refinements of $La_{1.2-x}Ln_{0.8}Sr_xCuO_{4+\delta}$ (Ln = Tb, Dy) [Space Group *P4/nmm* (No. 129), Z = 2]

	x, Ln, T (K)		
	0.03, Tb, 5	0.05, Tb, 5	0.20, Dy, 5
a (Å)	3.86404(2)	3.86234(2)	3.84217(3)
c (Å)	12.4477(2)	12.4453(2)	12.4988(4)
V (Å^3)	185.855(5)	185.655(5)	184.511(7)
La(1)/Sr			
z	0.38466(8)	0.38417(9)	0.38650(13)
$b_{11} = b_{22}$	0.0141(2)	0.0124(3)	0.0068(4)
b_{33}	0.00102(5)	0.00106(7)	0.00178(11)
$n_{La(1)}/n_{Sr}$	0.961(5)/0.03	0.937(6)/0.05	0.829(6)/0.20
La(2)/Tb or Dy			
z	0.09712(7)	0.09711(8)	0.10022(8)
$b_{11} = b_{22}$	0.0060(2)	0.0060(3)	0.0086(2)
b_{33}	0.00181(8)	0.00144(9)	0.00124(6)
$n_{La(2)}/n_{Tb}$	0.209(5)/0.82(2)	0.213(6)/0.81(2)	0.171(6)/0.79(1)
Cu			
z	−0.2450(2)	−0.2451(2)	−0.2442(3)
B_{iso} (Å^2)	0.44(3)	0.45(3)	0.38(5)
n	1.0	1.0	1.0
O(1)			
z	0.2393(2)	0.2393(2)	0.2391(5)
b_{11}	0.0211(9)	0.0202(11)	0.0109(15)
b_{22}	0.0070(8)	0.0068(10)	0.0018(15)
b_{33}	0.0034(1)	0.0034(1)	0.0045(3)
n	2.0	2.0	2.0
O(2)			
$x = y$	0.2933(5)	0.2906(6)	0.2831(11)
z	−0.4282(3)	−0.4286(4)	−0.4270(5)
B_{iso} (Å^2)	1.38(9)	1.39(11)	0.82(15)
n	1.0	1.0	1.0
O(3)			
$b_{11} = b_{22}$	0.0146(5)	0.0140(6)	0.0301(13)
b_{33}	0.0026(2)	0.0025(3)	0.0022(4)
n	1.0	1.0	1.0
O(4)			
z	0.538(4)	0.547(5)	—
B_{iso} (Å^2)	1.0	1.0	—
n	0.072(9)	0.056(11)	—
R_{wp}, R_{exp} (%)	8.2, 3.5	9.2, 4.9	8.1, 6.1
$R_{Mod(I)}$, R_{exp} (%)	3.7, 2.1	4.3, 2.7	5.1, 3.4

Note. The atoms were refined in the following positions of the unit cell: La(1)/Sr, La(2)/Tb and Cu in 2*c* (4*mm*): (1/4, 1/4, z), O(1) and O(4) in 4*f* (2*mm*.): (3/4, 1/4, z), O(2) in 8*j* (..*m*): (x, x, z), and O(3) in 2*a* ($\bar{4}m2$): (3/4, 1/4, 0).

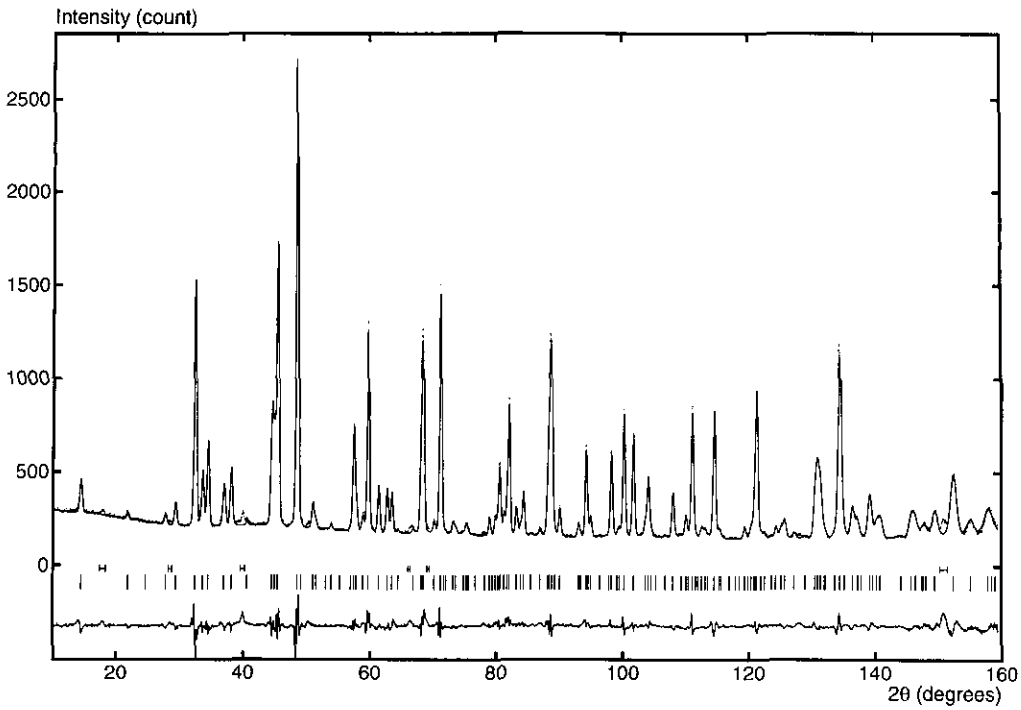

FIG. 5. Observed (points) and calculated (full curve) neutron diffraction profiles for $La_{1.17}Tb_{0.08}Sr_{0.03}CuO_{4+\delta}$ at 5 K. The reflection markers and the difference profile are also shown. Scattering from the cryostat is also marked.

0.538(4) and $n_{O(4)} = 0.074(8)$ and an improved fit quality ($R_{wp} = 0.082, R_I = 0.037$). Convergence to a true minimum was thoroughly tested by performing a series of refinements, in each case using different starting positions for the O(4) defect. No deviations from ideal stoichiometry were observed for the oxygen ions occupying normal lattice sites, discounting the possibility of the existence of vacancies ($n_{O(1)} = 2.01(1)$, $n_{O(2)} = 1.01(1)$, and $n_{O(3)} = 1.00(1)$). The final refined positional parameters are collected in Table 3 with selected bond lengths and angles in Tables 4–6. The observed, calculated, and difference profiles are shown in Fig. 5.

To complete our analysis, we also investigated two alternative defect models, but both were found inferior: (*a*) Part of the apical oxygen O(2) was kept in the "ideal" 2*c* site (1/4, 1/4, *z*), while the rest was *shifted* to O(5) in the 8*i* site (1/4, *y*, *z*), with $n_{O(2)} + n_{O(5)} = 1$. The oxygen defect O(4) was also introduced at the 4*f* sites as before. The refinement converged rapidly with marginally improved *R*-factors ($R_{wp} = 0.081$, $R_I = 0.037$) to $z_{O(2)} = -0.445(6)$, $n_{O(2)} = 0.16(3)$, and $y_{O(5)} = 0.326(4)$, $z_{O(5)} = -0.4248(9)$, $n_{O(5)} = 0.84(3)$. The O(4) defect positional and occupancy parameters ($z_{O(4)} = 0.539(4)$, $n_{O(4)} = 0.069(9)$) were not substantially affected. However, the meaningfulness of this refinement is questionable: if O(5) is distributed in the positions which maintain the longest O(5)–O(4) distance (2.64(3) Å), we expect a relationship $n_{O(5)} \leq 4 \times n_{O(4)}$ to hold for the occupancies of the two sites, i.e., the presence of the oxygen defect O(4) at the interstitial space of the rock-salt bilayers would result in the displacement of at most four apical oxygens from their "ideal" O(2) position (30, 32). In the present case, this ratio (~12) is not physically meaningful, while in addition, a short (La/Sr)–O(2) bond (2.12(8) Å) is present. (*b*) a Rietveld refinement was also performed with the assumption that the displaced O(5) oxygens were *shifted* to the more general 8*j* site (*x*, *x*, *z*), effectively allowing more "space" for the accommodation of the O(4) defect at its interstitial (3/4, 1/4, 0.538) position. We constrained the site occupancies, so that $n_{O(2)} + n_{O(5)} = 1$. The refinement did not affect the O(4) defect, while the parameters for O(2) and O(5) were: $z_{O(2)} = -0.439(6)$, $n_{O(2)} = 0.21(6)$ and $x_{O(5)} = 0.303(2)$, $z_{O(5)} = -0.425(1)$, $n_{O(5)} = 0.79(6)$. At the same time, virtually unchanged *R*-factors were obtained ($R_{wp} = 0.082$, $R_I = 0.037$). However, again an unrealistically large number (~12) of displaced O(5) atoms were obtained.

Finally, in a single crystal X-ray diffraction study of $La_{1.13}Tb_{0.81}Pb_{0.06}CuO_{4-\delta}$, the positional disorder of the apical O(2) sites were ascribed (33) to ordered *canting* of the CuO_5 pyramids, rather than to cation ordering in the La_2CuO_4 part of the T* unit cell. As a consequence, superstructure peaks were observed in this sample below 470 K, marking the onset of a transition to an orthorhombic phase. The space group $P2_1ma$ was found appropriate to describe the canting mechanism, resulting in two inequivalent crystallographic positions for each of the atoms La,

TABLE 4
Selected Bond Distances (Å) at 5 K for $La_{1.2-x}Ln_{0.8}Sr_xCuO_{4+\delta}$ (Ln = Tb, Dy)

x, Ln	0.03, Tb	0.05, Tb	0.20, Dy	N
	Host structure			
Cu–O(1)	1.9333(1)	1.9325(1)	1.9221(2)	4
Cu–O(2)	2.293(5)	2.294(5)	2.292(7)	1
La(1)/Sr–O(1)	2.647(2)	2.642(2)	2.662(4)	4
La(1)/Sr–O(2)	2.341(4)	2.341(5)	2.338(6)	1
	2.554(2)	2.570(3)	2.587(4)	1
	2.796(2)	2.795(3)	2.770(4)	2
	3.018(2)	3.004(3)	2.941(4)	1
La(2)/Ln–O(1)	2.621(2)	2.620(2)	2.589(4)	4
La(2)/Ln–O(3)	2.2791(4)	2.2782(5)	2.2934(5)	4
	Defect structure			
Cu–O(4)	3.32(4)	3.23(5)		
La(1)/Sr–O(4)	2.16(2)	2.11(3)		
	2.72(3)	2.80(5)		
O(2)–O(4)	2.51(3)	2.56(4)		

Note. N is the number of equivalent bonds.

Tb, Cu, O(1), and O(2). We thus also investigated the applicability of this model to $La_{1.17}Tb_{0.8}Sr_{0.03}CuO_{4+\delta}$. However, none of the superstructure peaks expected on the enlarged $a_T\sqrt{2} \times a_T\sqrt{2} \times c_T$ orthorhombic cell was present in our data. In particular, the (410) superstructure peak should have appeared at $2\theta \sim 74°$, in a range where the D2b diffractometer has maximum resolution; no such peak was present. The search for the (253) superstructure peak near $2\theta \sim 108°$ was also unsuccessful. In addition, Rietveld refinements with the $P2_1ma$ space group showed no stability. We thus conclude that an orthorhombically distorted structure is not suitable to describe the crystal properties of the present sample.

(*ii*) *Profile refinements of* $La_{1.15}Tb_{0.8}Sr_{0.05}CuO_{4+\delta}$ *and* $LaDy_{0.8}Sr_{0.2}CuO_{4-\delta}$. Structural models based on the one established for $La_{1.17}Tb_{0.8}Sr_{0.03}CuO_{4+\delta}$ were used in the refinement of the diffraction profiles of these oxides, collected at 5 K. In the case of $La_{1.15}Tb_{0.8}Sr_{0.05}O_{4+\delta}$,

TABLE 5
Selected Copper–Oxygen Bond Angles (°) for $La_{1.2-x}Ln_{0.8}Sr_xCuO_{4+\delta}$, Ln = Tb, Dy (T = 5 K)

x, Ln	0.03, Tb	0.05, Tb	0.20, Dy
O(1)–Cu–O(1)	89.92(1)	89.92(1)	89.94(1)
	175.80(17)	175.74(19)	176.19(34)
O(1)–Cu–O(2)	96.28(11)	96.04(13)	95.11(24)
	87.91(11)	88.21(13)	88.70(23)
O(2)–Cu–O(2)	8.37(6)	7.84(8)	6.41(13)
	11.85(6)	11.09(8)	9.07(13)

TABLE 6
Selected Oxygen–Oxygen Bond Distances (Å) in the CuO_5 Pyramids

T* phases	O(1)–O(1)	O(1)–O(2)
$La_{1.2}Tb_{0.8}CuO_{4.082(37)}$	2.7334(0)	2.999(20)
		3.194(21)
$La_{1.17}Tb_{0.8}Sr_{0.03}CuO_{4.072(9)}$	2.7323(0)	2.945(4)
		3.157(4)
$La_{1.15}Tb_{0.8}Sr_{0.05}CuO_{4.056(11)}$	2.7311(0)	2.953(5)
		3.151(5)
$LaDy_{0.8}Sr_{0.20}CuO_{4.00(3)}$	2.7168(0)	2.954(7)
		3.116(7)
$La_{1.2}Tb_{0.77}Ce_{0.03}CuO_{4.083(19)}$/5 K	2.7360(0)	2.937(4)
		3.168(4)
$La_{1.2}Tb_{0.77}Ce_{0.03}CuO_{4.064(21)}$/300 K	2.7390(0)	2.948(5)
		3.166(5)

the apical oxygens O(2) are "displaced" to the less symmetrical 8*j* sites (x, x, z), and refinement of the site occupancy of the 4*f* site (3/4, 1/4, z; z = 0.547(5)) reveals the presence of excess oxygen O(4) ($n_{O(4)}$ = 0.06(1)) at the interstitial space in the rock-salt $(La,Sr)_2O_2$ layers. Unconstrained refinement of the O(1), O(2), and O(3) site occupancies showed that none was oxygen-rich or oxygen-deficient ($n_{O(1)}$ = 2.02(2), $n_{O(2)}$ = 1.02(1), $n_{O(3)}$ = 1.01(1)). Occupancies of M and M' sites were allowed to vary, subject to the constraints of the overall nominal stoichiometry. The results of the refinement (R_{wp} = 0.092, R_I = 0.043) are presented in Table 3; the somewhat larger standard deviations and R-factors reflect the shorter counting time. Selected bond distances and angles are given in Tables 4–6.

The Rietveld refinement of the $LaDy_{0.8}Sr_{0.2}CuO_{4-\delta}$ powder diffraction data was initiated with ($La_{0.8}Sr_{0.2}$) on the M-sites (CN = 9) and ($Dy_{0.8}La_{0.2}$) on the M'-sites (CN = 8), according to the nominal stoichiometry of the sample. The displaced model for the apical O(2) oxygens resulted in good fit quality (R_{wp} = 0.081, R_I = 0.051). We note that as a result of the large bound incoherent scattering (σ_{inc} = 54.4 b) and absorption cross section (σ_{abs} = 994 b) of Dy, a rather poor signal-to-noise ratio resulted. Unlike the lightly doped oxides studied earlier, no convincing evidence for the presence of interstitial oxygen anions O(4) was found; its introduction led to no significant improvement of the fit and resulted in unphysically short metal–oxygen bond distances. We also could not detect any significant vacancy concentration for any of the oxygen sites (cf. the TGA estimate of the oxygen vacancy concentration as δ = 0.07(6)). The final structural parameters are presented in Table 3, and selected bond distances and angles in Tables 4–6. The observed, calculated, and difference profiles are shown in Fig. 6.

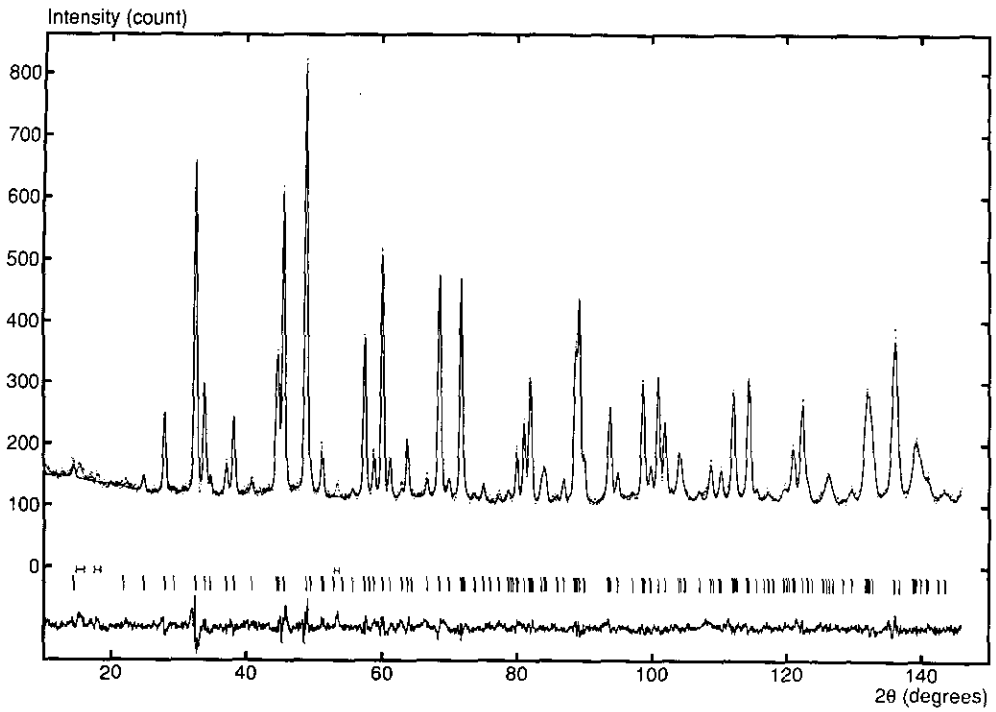

FIG. 6. Observed (points) and calculated (full curve) neutron diffraction profiles for $LaDy_{0.8}Sr_{0.2}CuO_{4-\delta}$ at 5 K. The reflection markers and the difference profile are also shown. Scattering from the cryostat is also marked.

(iii) Profile refinement of $La_{1.2}Tb_{0.77}Ce_{0.03}CuO_{4+\delta}$. Data with excellent statistics were collected between $10° \leq 160°$ at 5 and 300 K. No deviation from the tetragonal symmetry was observed at both temperatures. Refinement proceeded smoothly within the displaced O(2) model, discussed earlier. Site ordering of the cations at the M and M' sites was confirmed by performing refinements in which the total La and Ce content were kept fixed at 1.2 and 0.03, respectively. Uncontrained refinement of the Tb occupancy at the M' site converged to 0.80(2) at 5 K and 0.82(2) at 300 K, with La distributed between the two sites in the ratio $n_{La(1)} : n_{La(2)} = 0.964(5) : 0.236(5)$ at 5 K and $0.980(6) : 0.220(6)$ at 300 K. However, unlike the Sr^{2+}-doped systems, a series of exploratory refinements revealed that the apical oxygen O(2) 8*j* sites (x, x, z) were substoichiometric. Refinement at 5 K gave $n_{O(2)} = 0.96(1)$, $B_{iso} = 1.3(1)$ Å^2 ($R_{wp} = 0.090$, $R_I = 0.045$), while at room temperature $n_{O(2)} = 0.94(1)$, $B_{iso} = 1.5$ Å^2 ($R_{wp} = 0.101$, $R_I = 0.051$. This is reminiscent of the oxygen deficiency ($n_{O(2)} = 0.93(1)$) found at the same sites for both superconducting and nonsuperconducting T* $Nd_{1.32}Sr_{0.41}Ce_{0.27}CuO_{4-\delta}$ phases (30). Such evidence for deficiency at the 8*j* sites implies either that the *missing* oxygen is accommodated at interstitial sites or that *excess* oxygen anions are forming a defect, in a way similar to $La_2NiO_{4.18}$ (32) and $La_2Cu_{1-x}Co_xO_{4+\delta}$ (22). Clear evidence for the latter explanation was obtained when we introduced an O(4) interstitial defect and its site occupancy assumed significantly large values ($n_{O(4)} = 0.11(1)$). Consequently, the oxygen defect model was adopted in the final refinements, leading to significantly improved R-factors ($R_{wp} = 0.084$, $R_I = 0.037$ at 5 K; $R_{wp} = 0.094$, $R_I = 0.040$ at 300 K). The final structural parameters are presented in Table 7 and selected bond distances and angles in Tables 6, 8, and 9.

(iv) Profile refinement of $La_{1.2}Tb_{0.8}CuO_{4+\delta}$. The high-resolution time-of-flight data for $La_{1.2}Tb_{0.8}CuO_{4+\delta}$ unambiguously confirmed the tetragonal symmetry of the crystal structure. The profile lacked any indication of the presence of a superlattice (33) or broadened peaks which could be responsible for lowering the symmetry to orthorhombic. Rietveld refinements were performed on the basis of our earlier displaced O(2) model. Extra interstitial oxygen anions were introduced at the O(4) sites (3/4, 1/4, z); initially their z-coordinate was fixed to the value obtained for $La_{1.17}Tb_{0.8}Sr_{0.03}O_{4+\delta}$ ($z_{O(4)} = 0.538$) and only their occupancy was refined. The other oxygen sites (O(1), O(3)) were assumed to be "fully" occupied in accord with our earlier refinements. $z_{O(4)}$ was also included in the final stages of the refinement and convergence was achieved for $z_{O(4)} = 0.559(12)$ and $n_{O(4)} = 0.08(4)$. The parameters of our final structural model ($R_{wp} = 0.036$, $R_I = 0.031$) are presented in Table 7 and selected bond distances and angles in Tables 6, 8, and 9. The observed, calculated and difference profiles are shown in Fig. 7.

TABLE 7

Final Structural Parameters Derived from Rietveld Refinements of $La_{1.2}Tb_{0.8-x}Ce_xCuO_{4+\delta}$ (x = 0.0, 0.03) [Space Group *P4/nmm* (No. 129), Z = 2]

	x, Ln, T (K)		
	0.0, Tb, 4.2	0.03, Tb, 5	0.03, Tb, 300
a (Å)	3.86563(5)	3.86928(2)	3.87354(2)
c (Å)	12.4401(4)	12.4523(2)	12.4868(2)
V (Å^3)	185.893(10)	186.427(4)	187.355(4)
La(1)			
z	0.3850(6)	0.3855(2)	0.3852(2)
$b_{11} = b_{22}$	0.035(3)	0.0149(4)	0.0181(2)
b_{33}	0.0012(4)	0.0013(1)	0.0015(1)
n	1.0	0.991(5)	0.9792(1)
La(2)/Tb/Ce			
z	0.09767(5)	0.09774(4)	0.09742(5)
$b_{11} = b_{22}$	0.010(3)	0.0065(1)	0.0114(2)
b_{33}	3.0038(7)	0.00168(5)	0.00188(6)
$n_{La(2)}/n_{Tb}/n_{Ce}$	0.20/0.80	0.209(5)/0.80(2)/0.03	0.2208(1)/0.795(4)/0.03
Cu			
z	−0.2462(6)	−0.2452(2)	−0.2455(2)
B_{iso} (Å^2)	1.1(1)	0.46(3)	0.609(8)
n	1.0	1.0	1.0
O(1)			
z	0.2389(8)	0.2390(5)	0.2387(2)
b_{11}	0.029(4)	0.0228(9)	0.0248(11)
b_{22}	0.027(4)	0.0057(8)	0.0077(10)
b_{33}	0.0057(7)	0.0039(2)	0.0040(2)
n	2.0	2.0	2.0
O(2)			
$x = y$	0.289(6)	0.2971(5)	0.2944(6)
z	−0.432(1)	−0.4278(3)	−0.4274(4)
B_{iso} (Å^2)	3.6(6)	1.66(11)	1.81(14)
n	1.0	0.977(10)	0.962(11)
O(3)			
$b_{11} = b_{22}$	0.019(4)	0.0140(5)	0.0158(6)
b_{33}	0.0040(8)	0.0028(2)	0.0031(3)
n	1.0	1.0	1.0
O(4)			
z	0.559(12)	0.527(3)	0.527(3)
B_{iso} (Å^2)	1.0	1.0	1.2
n	0.082(37)	0.106(9)	0.102(10)
R_{wp}, R_{exp} (%)	3.6, 3.3	8.4, 2.7	9.4, 4.0
$R_{Mod(I)}$, R_{exp}/(%)	3.1, —	3.7, 1.5	4.0, 2.6

Note. The atoms were refined in the following positions of the unit cell: La(1), La(2)/Tb/Ce and Cu in 2*c* (4*mm*): (¼, ¼, *z*), O(1) and O(4) in 4*f* (2*mm*.): (¾, ¼, *z*), O(2) in 8*j* (..*m*): (*x*, *x*, *z*), and O(3) in 2*a* ($\bar{4}m2$): (¾, ¼, 0).

DISCUSSION

(*a*) *Conductivity*

The transport mechanism in the T* phases follows a variable-range-hopping (VRH) law over a relatively wide temperature range. The transport of charge carriers is thus limited by localized electronic states at the Fermi level. No indication of thermal activation of carriers from the Fermi energy to states at the conduction or valence bands was evident at high temperatures. Small polarons were found to move through the lattice by a thermally activated hopping process at $T > 100$ K only in the case of the heavily doped $LaDy_{0.8}Sr_{0.2}CuO_{4-\delta}$ sample.

In a similar fashion to covalent semiconductors like Ge or Si, we expect *impurity conduction* to occur in ionic semiconductors, such as $La_{1.2}Tb_{0.8}CuO_4$ and $La_{1.2}Dy_{0.8}CuO_4$, when a fraction of the lanthanide ions is replaced by an aliovalent element (e.g., doping with Sr^{2+} or Ce^{4+}). There is experimental evidence for such a behavior in related compounds, such as $La_2Cu_{1-x}Li_xO_{4-\delta}$ (34), $La_{2-x}Sr_xCuO_{4-\delta}$ (6), and $PrBa_2Cu_3O_{7-\delta}$ (35). Depending on whether the impurity cation has a higher or lower charge than La^{3+}, doping leads to donor or acceptor levels, situated in the gap just below the conduction or just above the valence band, respectively. The sharp donor or acceptor levels in the case of dilute impurities give rise to an impurity band as their concentration increases and their atomic orbitals gradually overlap. In the following, we illustrate our arguments assuming hole-doping, but the discussion is equally applicable in the case of electron-doping.

Formally, the impurity band is half-filled, when one hole is associated with each defect (e.g., Sr^{2+}) site. However, the on-site Coulomb interaction between holes splits the impurity band into two subbands separated by the correlation energy, U. The situation then for the T* phases can be approximated by the lower and upper Hubbard impurity subbands being occupied and unoccupied, respectively, and separated by a Hubbard gap as long as the bandwidth, W is smaller than the correlation energy, U. They then behave as Mott–Hubbard insulators. Simple calculations based on the "hydrogenic" model (where carriers are bound to the inpurity atoms in hydrogen-like orbitals, a common assumption in amorphous semiconductors) for impurity states, suggests that the Hubbard gap (given by the screened Coulomb repulsion between two carriers in the same impurity orbital: $U = (5/8)(e^2/4\pi\varepsilon_0\varepsilon_r\xi)$, where ξ is a measure of the spatial extent of the wave function localized at a single site and ε_r is the average relative permittivity of the material) should be comparable to the energy required to excite a hole from the impurity state into the valence band. Thus, the upper Hubbard subband probably overlaps with the valence band.

At higher dopant concentrations, the impurity band broadens and the two Hubbard subbands overlap. In the case of a perfectly ordered solid, a transition to a metallic state will occur. However, in doped compounds, strong disorder arising from randomly distributed impurities may result in two regimes in the density of states: extended states at the band center due to strong overlap of orbitals, and states localized at the band edges due to weak overlap ("Anderson" localization). The limit between localized and delocalized states is quite sharp and known as the *mobility edge*. Thus, when the upper Hubbard band overlaps weakly with the valence band, the Fermi energy may lie near the localized side of the mobility edge, resulting in a localized condensed hole gas. Then nonmetallic be-

TABLE 8
Selected Bond Distances (Å) for $La_{1.2}Tb_{0.8-x}Ce_xCuO_{4+\delta}$ (x = 0.0, 0.03).

	$La_{1.2}Tb_{0.8}CuO_{4+\delta}$ (4.2 K)	$La_{1.2}Tb_{0.77}Ce_{0.03}CuO_{4+\delta}$ (5 K)	$La_{1.2}Tb_{0.77}Ce_{0.03}CuO_{4+\delta}$ (300 K)	N
		Host structure		
Cu–O(1)	1.9348(6)	1.9362(1)	1.9386(2)	×4
Cu–O(2)	2.333(19)	2.288(5)	2.284(6)	×1
La(1)–O(1)	2.651(9)	2.659(2)	2.664(3)	×4
La(1)–O(2)	2.273(19)	2.339(5)	2.353(6)	×1
	2.582(22)	2.534(2)	2.551(3)	×1
	2.806(22)	2.798(2)	2.800(3)	×2
	3.014(22)	3.040(2)	3.028(3)	×1
La(2)/Tb/Ce–O(1)	2.624(8)	2.615(2)	2.620(2)	×4
La(2)/Tb/Ce–O(3)	2.276(4)	2.2856(3)	2.2871(3)	×4
		Defect structure		
Cu/O(4)	3.05(12)	3.43(3)	3.44(3)	
La(1)–O(4)	2.04(5)	2.22(2)	2.23(2)	
	2.94(12)	2.62(2)	2.62(3)	
O(2)–O(4)	2.65(10)	2.46(2)	2.45(2)	

Note. N is the number of equivalent bonds.

havior is expected, with the conductivity dominated by holes jumping between sites localized on opposite sides of the Fermi energy according to the *variable-range-hopping* mechanism (Eq. [4]). With further increase in doping, the upper Hubbard subband should merge with the valence band and an insulator-to-metal transition should take place.

However, such a transition was not observed for the $La_{1.2-x}Tb_{0.8-y}Sr_xCe_yCuO_{4+\delta}$ (Sr^{2+} or Ce^{4+} doped) and $LaDy_{0.8}Sr_{0.2}CuO_{4-\delta}$ compositions studied. These materials behave as Mott–Hubbard insulators, as both strontium (and cerium) dopants, and oxygen defects act as strong sources of localizing potential. The dimensionality (d) of the variable range-hopping conduction mechanism was determined from the experimental data using the $1/T^{\nu}$ dependence of the resistivity. The exponent $\nu = 1/(d+1)$ was found to be close to 1/3 for $La_{1.2}Tb_{0.8}CuO_{4+\delta}$ and its lightly doped derivatives, indicating that "anisotropic" two-dimensional (2D) hopping is dominating the conduction process between 150 and 315 K. With significantly increased carrier density in $LaDy_{0.8}Sr_{0.2}CuO_{4-\delta}$, a crossover to an "isotropic" three-dimensional (3D) hopping process was evident at $T \leq 100$ K. VRH is a percolation process and hence the resistivity is determined by the least resistive percolation path through the sample. In insulating T* phases, transport carriers are primarily confined to the CuO_2 layers. In the more conducting $LaDy_{0.8}Sr_{0.2}CuO_{4-\delta}$ sample, the percolation path for the carriers can be completed in interlayer directions as well.

The interpretation of the conductivity behavior is usually performed in terms of the localization length, ξ, which is a measure of the spatial extent of the wavefunction localized at a single site. The magnitude of ξ shows how close the system is to the insulator-to-metal transition, since divergent behavior is expected close to the transition. The average energy separating localized states is given by the quantity $k_B T_0$, which is readily calculated ($\sim 10^7$ K) from the temperature dependence of the measured resistances (Eq. [4]). The corresponding values in La_2CuO_4 and in amorphous semiconductors are $\sim 10^6$ and $\sim 10^8$ K, respectively. Using the results of electronic band structure calculations on the T* phases (36) to estimate the 2D density-of-states at the Fermi level as $\tilde{N}(E_F) = 8.6 \times 10^{14}$ states $eV^{-1}cm^{-2}$, and the 3D-DOS as $N(E_F) = 9 \times 10^{21}$ states $eV^{-1}cm^{-3}$ and the values of T_0 given in Table 2, we estimate an average ξ of ~0.25 Å in $La_{1.2-x}Tb_{0.8-y}Sr_xCe_yCuO_{4+\delta}$ (x = 0.0, 0.01, 0.03, 0.05 or y = 0.01, 0.03) and ~1.3 Å in $LaDy_{0.8}Sr_{0.2}CuO_{4-\delta}$. This

TABLE 9
Selected Copper–Oxygen Bond Angles (°) for $La_{1.2}Tb_{0.8-x}Ce_xCuO_{4-\delta}$ (x = 0.0, 0.03).

	$La_{1.2}Tb_{0.8}CuO_{4+\delta}$ (4.2 K)	$La_{1.2}Tb_{0.77}Ce_{0.03}CuO_{4+\delta}$ (5 K)	$La_{1.2}Tb_{0.77}Ce_{0.03}CuO_{4+\delta}$ (300 K)
O(1)–Cu–O(1)	89.88(3)	89.91(1)	89.89(1)
	174.75(62)	175.47(17)	175.02(20)
O(1)–Cu–O(2)	96.46(65)	96.83(11)	96.80(14)
	88.77(65)	87.69(11)	88.16(13)
O(2)–Cu–O(2)	7.69(64)	9.14(6)	8.64(8)
	10.89(65)	12.93(6)	12.23(8)

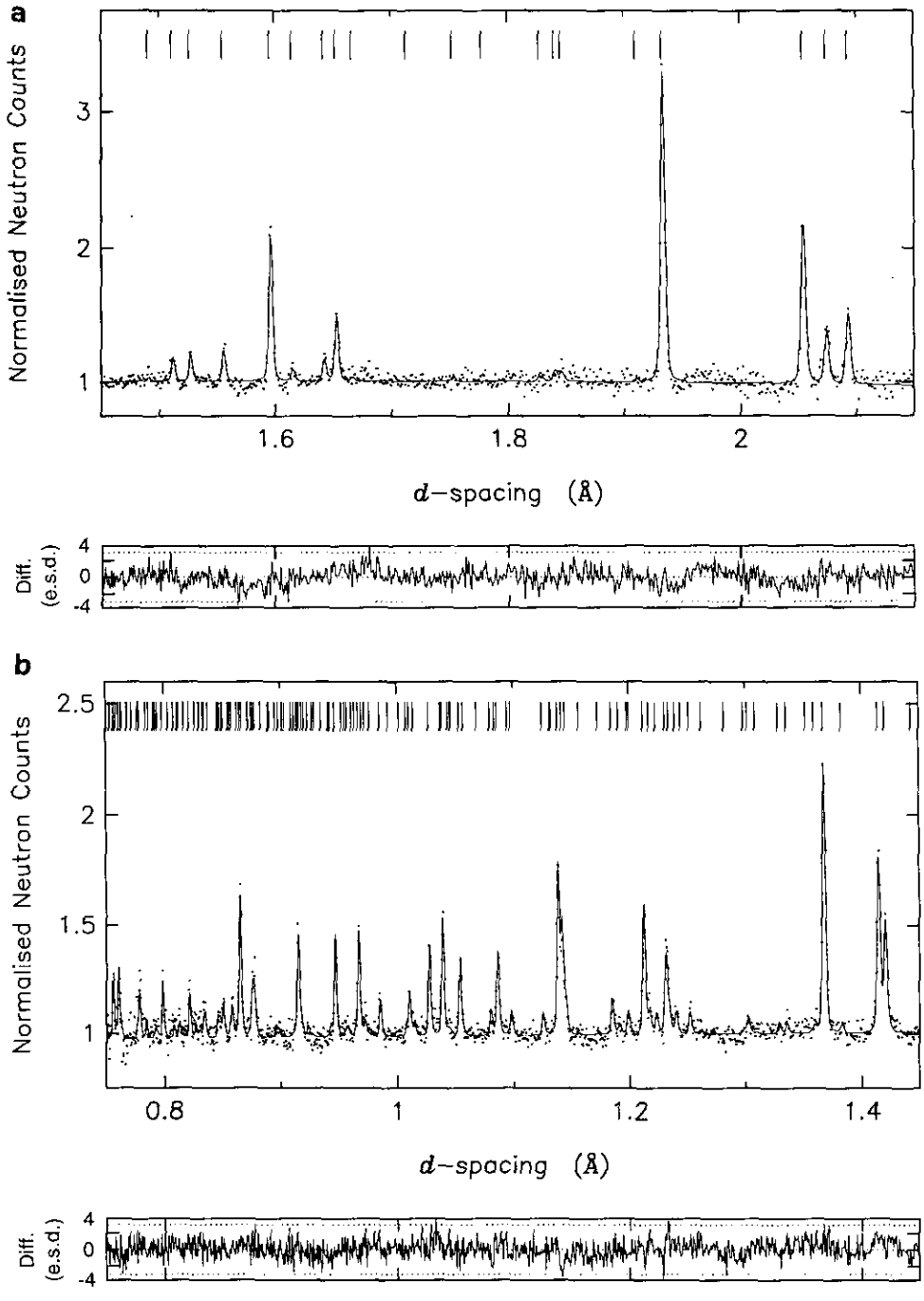

FIG. 7. Observed (points), calculated (full curve), and difference (bottom panel) time-of-flight neutron diffraction profiles for $La_{1.2}Tb_{0.8}CuO_{4+\delta}$ at 4.2 K: (a) 1.45 Å $< d <$ 2.15 Å, (b) 0.75 Å $< d <$ 1.45 Å. The reflection markers are also shown. The dotted lines in the difference profile panels are at $\pm 3\ \sigma$.

indicates that the percolation pathway confines the carriers essentially within the boundaries of the unit cell for all compositions, in contrast to La_2CuO_4, in which ξ assumes a value of ~4 Å (6), and then rapidly increases upon hole-doping as the insulator-to-metal transition is approached.

Finally, we comment on the observed small-polaron behavior in $LaDy_{0.8}Sr_{0.2}CuO_{4-\delta}$ between 100 and 315 K. Given the strong electron-lattice interactions of the charge carriers in the cuprates, polaronic effects are expected to be present, arising from the strong coupling of the extra charge with the polarization field of the lattice (37). The

charge produces some deformation of its surroundings and becomes trapped in the resulting local electrostatic potential. In $LaDy_{0.8}Sr_{0.2}CuO_{4-\delta}$, thermally activated hopping (Eq. [3]) of holes between traps is thus preferred as long as the temperature is quite high, but gives way to VRH (Eq. [4]) at lower temperatures.

(*b*) *Structural Considerations*

The crystal structure of the mixed-lanthanide cuprates $La_{1.2-x}Tb_{0.8}Sr_xCuO_{4+\delta}$, $LaDy_{0.8}Sr_{0.2}CuO_{4-\delta}$, and $La_{1.2}Tb_{0.8-y}Ce_yCuO_{4+\delta}$ (T* structural type), studied in the present work differs markedly from that of the related $La_{2-x}Sr_xCuO_{4-\delta}$ (O/T) and $Nd_{2-y}Ce_yCuO_{4-\delta}$ (T′) series of superconductors. The stability of these phases derives from the difference in size between the lanthanides present (i.e., La^{3+} and Tb^{3+} or Dy^{3+}). Essentially perfect ordering of the rare-earth elements occurs; the smaller ions (Tb^{3+}, Dy^{3+}) reside in eight-coordinate (M') sites within fluorite-type $(M'_2O_2)^{2+}$ layers and the larger ions (La^{3+}) in nine-coordinate (M) positions within rock-salt type $(M_2O_2)^{2+}$ layers. Thus half of the T′ and half of the (T/O) structural motifs fuse together to give a hybrid T* structure. The resulting coordination number of copper is 5. Furthermore, in agreement with the doping preferences of the T and T′ phases, Sr^{2+} doping occurs at the M sites, while Ce^{4+} doping leads to occupation of the smaller M' site.

The stability of layer perovskites with the T and T′ structures has been accounted for by using arguments based on tolerance factors (38), defined by the relationship

$$t = \frac{R_{Ln-O}}{\sqrt{2}\,R_{Cu-O}}, \qquad [5]$$

where R_{Ln-O} and R_{Cu-O} are the sums of the ionic radii for Ln and Cu cations and the oxide ion in the appropriate n-fold coordination. Thus the crystal chemistry of the relevant layered cuprate family can be discussed in terms of the matching of the copper–oxygen and lanthanide–oxygen bond distances in adjacent layers, with tolerance factors within the limits $0.85 < t < 1.02$ corresponding to good matching. Smaller values of t will lead to structural distortions with minimization of the bond length mismatch. We can also apply these arguments to the T* phases. In $La_{1.2}Tb_{0.8}CuO_{4+\delta}$, the calculated tolerance factors for the T and T′ halves of the unit cell, using the Shannon–Prewitt ionic radii, are $t_T = 0.90$ and $t_T' = 0.89$, respectively. Tolerance factors calculated using the experimentally determined bond lengths are even larger: $t_T = 0.97$ and $t_T' = 0.96$. Both values are very close to 1 and demonstrate the stability toward structural distortions of the T* unit cell. This excellent bond-length matching is in agreement with the structural results which show no deviations from tetragonal symmetry.

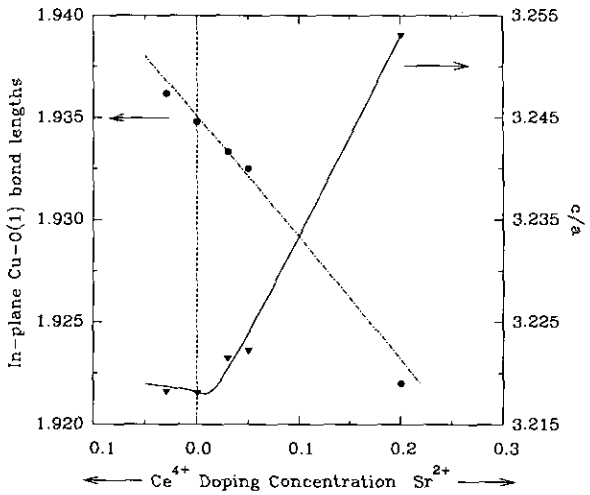

FIG. 8. Variation of the basal plane Cu–O(1) bond lengths (Å) and the lattice constant (c/a) ratio on doping.

The hybrid nature of the T* unit cell leads to a coexistence of compressive and tensile stresses on the CuO_2 layers, that compete for the optimum adjustment of the in-plane bond lengths. As a result, the basal plane Cu–O bond lengths in the T* phases (~1.93 Å) are found to be longer than those in the T phases (~1.90 Å), but shorter than the ones in T′ phases (~1.96 Å). These structural considerations will also influence the way doping will occur in the present systems: p-type doping should effectively relieve the compressive pressure on the CuO_2 sheets originating from the T-like part of the unit cell, while n-type doping should reduce the tensile pressure, now coming from the T′ part. Our structural data are consistent with these ideas. Ce^{4+} ions are found to be accommodated at the M' sites, while partial substitution of La^{3+} by the larger and more basic Sr^{2+} ion leads to a tolerance factor increase and stabilization of the La_2CuO_4 part of the intergrowth structure.

Figure 8 presents the variation with Sr^{2+} and Ce^{4+} doping of both the in-plane Cu–O(1) bonds and the tetragonal axes (c/a) ratio. Reduction of the basal plane dimensions as required by hole doping dominates over the size effect of the Sr^{2+} ions, which favors an expanded basal plane; then a smooth decrease in the Cu–O(1) bond length is observed with increasing Sr^{2+} content. The c-axis also becomes longer and the c/a ratio shows a smooth increase upon oxidation. The behavior of the c/a ratio for $La_{1.2}Tb_{0.77}Ce_{0.03}CuO_{4+\delta}$ is somewhat unexpected, in that it remains essentially unchanged upon doping: c/a = 3.21825(7) for $La_{1.2}Tb_{0.77}Ce_{0.03}CuO_{4+\delta}$, compared to c/a = 3.21813(14) for $La_{1.2}Tb_{0.8}CuO_{4+\delta}$. This behavior may be understood if we recall that excess oxygen anions

[$<\delta> \sim 0.07(2)$] were found in the unit cell of $La_{1.2}Tb_{0.77}Ce_{0.03}CuO_{4+\delta}$. Within the formalism of our "oxygen defect" model, such oxygen is accommodated in the interstitial space defined by the rock-salt type (Ln_2O_2) layers. The lattice site occupied is close to the larger vacant place of the unit cell, and is coordinated by four *Ln*(1) and four *c*-axis oxygens O(2). The defect geometry is consistent with a negatively charged O^{2-} ion, which will compensate for the electron doping resulting from the Ce^{4+} ions. The effective expansion of the $Ln_2O_{2+\delta}$ rock-salt layers due to the presence of the O^{2-} defect thus competes with the *c*-axis contraction due to partial Ce^{4+} substitution at the *M'* sites and an unchanged *c*/*a* ratio results.

It has been widely accepted that formation of the T* phases is extremely sensitive to oxygen fugacity (16) and the role of oxygen for the appearance of superconductivity in the T* phases has been also stressed (20). For high levels of hole doping, samples prepared at ambient pressure (e.g., $La_{1.8-x}Ln_xSr_{0.2}CuO_{4-\delta}$, *Ln* = Sm, Eu, Gd) contained a sizable number of oxygen vacancies. This necessitated high-pressure oxygen annealing to lead to superconductivity. In sharp contrast, T* samples containing Tb and Dy ions did not show superconductivity even under high-pressure oxygenation (15), possibly because the oxygen vacancies are not eliminated, and thus the effective hole concentration is not raised. Moreover, it was suggested (20) that T_c is suppressed with decreasing lanthanide size (from Sm^{3+} to Dy^{3+}) due to enhanced *local structural disorder*, caused by strain due to size mismatch and possible distortion of the oxygen configuration.

The TGA measurements of $LaDy_{0.8}Sr_{0.2}CuO_{4-\delta}$ indicate the presence of oxygen vacancies ($\delta \sim 0.06$) in this material with some corraborative weak evidence from the Rietveld analysis of the powder neutron diffraction data. On the other hand, both $La_{1.2}Tb_{0.8}CuO_{4+\delta}$ and its lightly doped derivatives $La_{1.2-x}Tb_{0.8}Sr_xCuO_{4+\delta}$ (x = 0.03, 0.05) and $La_{1.2}Tb_{0.77}Ce_{0.03}CuO_{4+\delta}$ easily accommodate excess oxygen in the form of O^{2-} defects, without the need of high oxygen pressure synthesis. Figure 9 shows that the oxygen uptake is gradually reduced as the Sr^{2+} doping level increases. The lack of metallic and superconducting properties in these materials may arise from the compensating effects of Tb mixed valency. This was for example evident in X-ray absorption measurements of $La_{0.9}Tb_{0.9}Sr_{0.2}CuO_4$ (20) at the Tb L_3 edge with ~20% of the Tb ions being present at an oxidation state greater than 3+. If Tb^{4+} ions exist at the eight-coordinate (*M'*) sites, their amount will play an important role in compensating for hole doping and maintaining the carrier concentration below a value essential to induce metallic or superconducting character. This behavior is more pronounced at low levels of extrinsic doping (e.g., Sr^{2+}), where self doping by oxygen uptake seems to be needed to equilibrate the extra charge due to Tb oxidation states >3+.

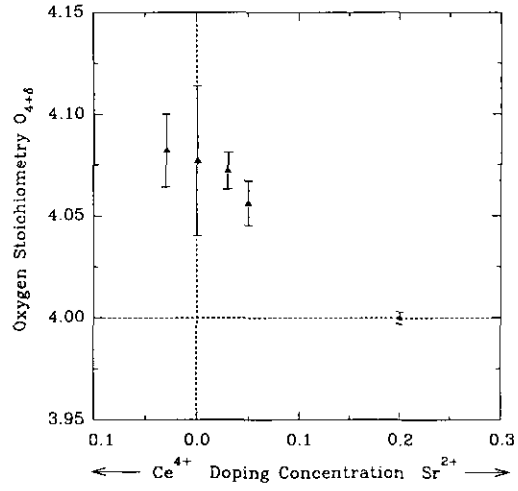

FIG. 9. Variation of the excess oxygen uptake in the T* phases as determined by means of the Rietveld analysis technique.

The present structural data indicate that the oxygen defect found in formally undoped $La_{1.2}Tb_{0.8}CuO_{4+\delta}$ plays an important role for the stabilization of the T* intergrowth structure. This may be intrinsic to the behavior of T* compounds containing smaller rare-earths (Tb, Dy) which form a T* phase without any doping. Indeed, when deviations from an optimum average rare-earth ionic radius occur, an adjustment of the oxidation state through oxygen uptake occurs, leading to stabilization of the T* structure. For instance, in $La_{1.2}Tb_{0.8}CuO_4$, if the (La, Tb) ionic radius exceeds an optimum value for perfect bond length matching, oxygen uptake can affect the stabilization of the T* phase by oxidizing some Tb^{3+} ions, thus reducing the average (La, Tb) ionic radius. This may be contrasted by the lack of "undoped" T* phase formation in the compounds containing intermediate size rare-earths (Sm, Eu, Gd), where extension of the T* homogeneity range is achieved only with Sr addition.

CONCLUSIONS

We have presented structural and transport measurements on a series of T* phases $La_{1.2-x}Tb_{0.8-y}Sr_xCe_yCuO_{4+\delta}$ (x = 0.0, 0.01, 0.03, 0.05 or y = 0.01, 0.03) and $La Dy_{0.8}Sr_{0.2}CuO_{4-\delta}$. The structural variation of the T* phases with dopant concentration and temperature can be rationalized in terms of tolerance-factor arguments, based on the mismatch in size between the lanthanide bilayers and the CuO_2 planes. Optimum bond length matching in the copper and rare-earth coordination environments, with the fusion of half of the T/O and half of the T' structural motifs, leads to a tolerance factor which favors no distortion of the tetragonal unit cell. High resolution powder neutron diffraction measurements found

T* to be free of tilting distortions, adopting the tetragonal *P4/nmm* symmetry down to low temperatures. The peculiarity of the Tb containing materials to favor excess interstitial oxygen anions in their crystal structure was understood in terms of the existence of some small fraction of Tb ions in oxidation states greater than 3+. Such an oxygen incorporation was found to play a stabilizing role in the T* phase formation at low Sr^{2+} doping levels, with the oxygen uptake diminishing at higher degrees of oxidation.

Conductivity measurements showed the dominant role of a two-dimensional (2D) variable-range-hopping (VRH) mechanism across the present series, thus suggesting that localized states exist near the Fermi energy (E_F). A crossover from 2D- to 3D-VRH was found with increased carrier density in the heavily doped Dy phase at low temperatures, whereas small-polaron behavior dominated its conductivity at higher temperatures. This behavior was discussed on the basis of impurity band conduction in classical amorphous semiconductors, effectively resulting in a Mott–Hubbard insulator with the carriers hopping between localized states close to E_F.

ACKNOWLEDGMENTS

We acknowledge financial support by the Science and Engineering Research Council (United Kingdom) and the European Community (Brite-EURAM program). Access to neutron facilities at the Institut Laue–Langevin, Grenoble, France and the Rutherford Appleton Laboratory, Oxon, United Kingdom is also gratefully acknowledged. We thank J. K. Cockcroft and R. M. Ibberson for help with the experiments.

REFERENCES

1. P. Day, M. J. Rosseinsky, K. Prassides, W. I. F. David, O. Moze, and A. Soper. *J. Phys. C* **20,** L429 (1987).
2. M. J. Rosseinsky, K. Prassides, and P. Day. *Physica C* **161,** 21 (1989).
3. H. Sawa, S. Suzuki, M. Watanabe, J. Akimitsu, H. Matsubara, H. Watab, S. Uchida, K. Kokusho, H. Asano, F. Izumi, and E. Takayama-Muromachi, *Nature* **337,** 347 (1989).
4. J. Beille, B. Chevalier, G. Demazeau, F. Deslandes, J. Etourneau, O. Laborde, C. Michel, P. Lejay, J. Provost, B. Raveau, A. Sulpice, J. L. Tholence, and R. Tournier, *Physica B* **146,** 307 (1987).
5. R. J. Birgeneau and G. Shirane, *in* "Physical Properties of High Temperature Superconductors" (D. M. Ginsberg, Ed.). World Scientific, London, 1989.
6. M. J. Rosseinsky, K. Prassides, and P. Day, *J. Mater. Chem.* **1,** 597 (1991).
7. M. J. Rosseinsky, K. Prassides, and P. Day, *Inorg. Chem.* **30,** 2680 (1991).
8. V. B. Grande, H. Müller-Buschbaum, and M. Schweizer, *Z. Anorg. Allg. Chem.* **428,** 1201 (1977).
9. J. D. Axe, A. H. Moudden, D. Hohlwein, D. E. Cox, K. M. Mohanty, A. R. Moodenbaugh, and Y. Xu, *Phys. Rev. Lett.* **62,** 2751 (1989).
10. J. D. Jorgensen, B. Dabrowski, S. Pei, D. G. Hinks, L. Soderholm, B. Morosin, J. E. Schirber, E. L. Venturini, and D. S. Gingley, *Phys. Rev. B* **38,** 11337 (1988).
11. H. Müller-Buschbaum and W. Wollschlager, *Z. Anorg. Allg. Chem.* **414,** 76 (1975).
12. M. J. Rosseinsky and K. Prassides, *Europhys. Lett.* **14,** 551 (1991).
13. E. Takayama-Muromachi, Y. Matsui, Y. Uchida, F. Izumi, M. Onoda, and K. Kato, *Jpn. J. Appl. Phys.* **27,** L2283 (1988).
14. T. Kenjo and S. Yajma, *Bull. Chem. Soc. Jpn.* **50,** 2847 (1977).
15. S.-W. Cheong, Z. Fisk, J. D. Thompson, and R. B. Schwartz, *Physica C* **159,** 407 (1989).
16. J. F. Bringley, S. S. Trail, and B. A. Scott. *J. Solid State Chem.* **86,** 310 (1990).
17. Y. K. Tao, Y. Y. Sun, J. Paredes, P. H. Hor, and C. W. Chu, *J. Solid State Chem.* **82,** 176 (1989).
18. A. Lappas, K. Prassides, A. Amato, R. Feyerherm, F. N. Gygax, and A. Schenck, *Hyperfine Interact.* **86,** 555 (1994).
19. A. Lappas, K. Prassides, A. Amato, R. Feyerherm, F. N. Gygax, and A. Schenck, in preparation.
20. Z. Tan, J. I. Budnick, S. Luo, W. Q. Chen, S-W Cheong, A. S. Cooper, P. C. Canfield, and Z. Fisk, *Phys. Rev. B* **44,** 7008 (1991).
21. F. C. Chou, J. H. Cho, L. L. Miller, and D. C. Johnston, *Phys. Rev. B* **42,** 6172 (1990).
22. A. Lappas and K. Prassides, *J. Solid State Chem.* **108,** 59 (1994).
23. P. Bordet, J. J. Capponi, C. Chaillout, S.-W. Cheong, J. Chenavas, Z. Fisk, T. Fournier, J. L. Hodeau, D. B. McWhan, A. Varela-Losada, and M. Marezio, *J. Less-Common Met.* **164–165,** 792 (1990).
24. A. W. Hewat, personal communication.
25. H. M. Rietveld, *J. Appl. Crystallogr.* **2,** 65 (1969).
26. J. K. Cockcroft, "Program PROFIL." Birkbeck College, London, 1993.
27. I. G. Austin and N. F. Mott, *Adv. Phys.* **18,** 41 (1969).
28. N. F. Mott, *Philos. Mag.* **19,** 835 (1969).
29. B. I. Shklovskii and A. L. Efros, "Electronic Properties of Doped Semiconductors." Springer-Verlag, Berlin, 1984.
30. F. Izumi, E. Takayama-Muromachi, Y. Nakai, and H. Asano, *Physica C* **157,** 89 (1989).
31. P. Lightfoot, S. Pei, J. D. Jorgensen, X.-X. Tang, A. Manthiram, and J. B. Coodenough, *Physica C* **169,** 15 (1990).
32. J. D. Jorgensen, B. Dabrowski, S. Pei, D. R. Richards, and D. G. Hinks, *Phys. Rev. B* **40,** 2187 (1989).
33. P. Bordet, S.-W. Cheong, Z. Fisk, T. Fournier, J. L. Hodeau, M. Marezio, A. Santoro, and A. Valera, *Physica C* **171,** 468 (1990).
34. M. A. Kastner, R. J. Birgeneau, C. Y. Chen, Y. M. Chiang, D. R. Gabbe, H. P. Jenssen, T. Junk, C. J. Peters, P. J. Picone, T. Thio, T. R. Thurston, and H. L. Tuller, *Phys. Rev. B* **37,** 111 (1988).
35. B. Fisher, G. Koren, J. Genossar, L. Patlagen, and E. L. Gartstein, *Physica C* **176,** 75 (1991).
36. G. Y. Guo, Z. Szotek, and W. M. Temmerman, *Physica C* **102–104,** 1351 (1989); Z. Szotek, G. Y. Guo, and W. M. Temmerman, *Physica C* **175,** 1 (1991).
37. L. J. de Jongh, *in* "Mixed Valency Systems: Applications in Chemistry, Physics and Biology" (K. Prassides, Ed.), p. 223. Kluwer Academic, Dordrecht 1991.
38. P. Ganguly and C. N. R. Rao. *J. Solid State Chem.* **53,** 193 (1984).